

Tuning for fluidity using fluctuations in biological tissue models

Sadjad Arzash,^{1,2} Indrajit Tah,³ Andrea J. Liu,² and M. Lisa Manning¹

¹*Department of Physics, Syracuse University, Syracuse, NY 13244, USA*

²*Department of Physics and Astronomy, University of Pennsylvania, Philadelphia, PA 19104, USA*

³*Speciality Glass Division, CSIR-Central Glass and Ceramic Research Institute, Kolkata 700032, India*

How do biological systems tune emergent properties at the scale of tissues? One class of such emergent behaviors, important to biological functions such as body-axis elongation, involves rigidity transitions, in which a tissue changes from a fluid-like state to a solid-like state or vice versa. Here, we explore the idea that tissues might tune “learning degrees of freedom” to affect this emergent behavior. We study tissue fluidity in the 2D vertex model, using the vertex model energy as a learning cost function and the cell stiffnesses, target shapes, and target areas as sets of learning degrees of freedom that can be varied to minimize the energy. We show that the rigidity transition is unaffected when cell stiffnesses are treated as learning degrees of freedom. When preferred perimeters or areas are treated as learning degrees of freedom, however, energy minimization introduces spatial correlations in target cell shapes or areas that shift the rigidity transition. There is an optimal heterogeneity of target cell shapes or areas to enable learning. These observations suggest that biological tissues can learn tissue-scale behaviors by tuning their individual cell properties.

Instructions for constructing biological tissues are encoded at the scale of molecules but drive collective tissue behavior at the multicellular scale. Similarly, in systems such as mechanical, flow or electrical networks, instructions encoded in microscopic structure are responsible for collective properties. An effective strategy for solving the inverse problem of material design in these networks is gradient descent on a *learning cost function* that embodies the desired collective property by tuning microscopic *learning degrees of freedom*, such as the presence or absence of a bond, bond stiffnesses or rest lengths in elastic networks, or conductances in flow or electrical networks [1]. Physics dictates that each system must also satisfy physical constraints during learning, imposed by minimizing the *physical cost function* (energy in elastic networks or dissipated power in flow or electrical networks) with respect to *physical degrees of freedom* (node positions in elastic networks, node pressures/voltages in flow/electrical networks). Simultaneous minimization of physical and learning cost functions with respect to physical and learning degrees of freedom can be used to generate an auxetic [2–4] or allosteric response [1, 5]. Alternatively, minimization of physical cost functions while varying learning degrees of freedom according to local rules [6] can also be effective. Such local update rules include those that naturally occur in real materials, like directed aging [7–9], as well as rules that approximate gradient descent, as in Equilibrium Propagation [10] or Coupled Learning [11]. These ideas have led to successful learning of desired properties in the lab [1, 7, 8, 12–14].

Here we explore the idea that biological epithelial tissues might tune cell-scale properties, viewed as learning DOF, to drive robust macroscopic, collective behaviors necessary for development and evolution. A well-vetted class of simple biophysical models (vertex [15–18], Voronoi [19], and cellular Potts [20] models) successfully captures a fluid-to-solid transition controlled by cell

shape. Recent work demonstrates that tissues must shift from a solid to a fluid [21, 22] or near-fluid [23] state as a function of space [21] and time [22], to facilitate flows necessary for body axis elongation [21–23] and organ formation [24, 25]. Perhaps these developmental processes can usefully be regarded as learning processes, in which cell-scale learning DOF are adjusted to develop observed tissue-scale behaviors.

This viewpoint is bolstered by the recent finding that the *Drosophila* amnioserosa appears to shift its rigidity transition to remain rigid throughout the developmental process of dorsal closure by tuning preferred cell shapes continuously throughout the process [26]. Here we investigate how learning DOF affect the fluid-solid transition in 2D vertex models more generally, to guide future searches for active learning mechanisms in epithelial tissues. We investigate how different sets of allowed learning DOF – specifically, cell stiffnesses, preferred areas, or preferred perimeters – affect tissue rigidity. In contrast to Ref. [26], where the rigidity transition trivially shifts due to the changing average of the learning DOF distribution, we fix the distribution or a set of its moments to ask the more subtle question of whether *spatial correlations* of learning DOF introduced by minimization of a cost function are sufficient to shift the rigidity transition.

We study a 2D vertex model [16, 27], which describes a tissue monolayer as a network of polygonal cells. The physical DOF are the polygon vertices. Cellular properties and interactions are encoded in an energy function $E = \sum_i^N [K_{A,i}(A_i - A_{0,i})^2 + K_{P,i}(P_i - P_{0,i})^2]$, where A_i and $A_{0,i}$ are the actual and preferred areas, P_i and $P_{0,i}$ are the actual and preferred perimeters, $K_{A,i}$ and $K_{P,i}$ are the area and perimeter moduli of cell i . It is helpful to make the above equation dimensionless using $\langle K_{A,i} \rangle \langle A_{0,i} \rangle^2$ as the units of energy and $\sqrt{\langle A_{0,i} \rangle}$ as the

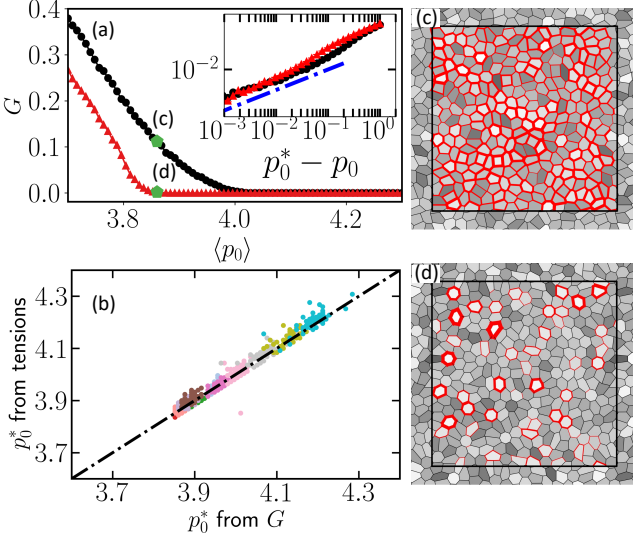


FIG. 1. (a) Shear modulus G versus average target shape $\langle p_0 \rangle$ in vertex models with polydisperse $p_{0,i}$. Black curve (circles) shows minimization based solely on physical degrees of freedom, while red curve (triangles) includes both physical and $\{p_{0,i}\}$ degrees of freedom. Inset illustrates shear modulus scaling; dashed blue line indicates a slope of 1.0. (b) Rigidity transition point p_0^* from edge tension percolation versus shear modulus G with different σ values for $\{p_{0,i}\}$ as degrees of freedom (DOF). Black dashed line represents $y = x$. (c, d) Tissue structures for highlighted points in (a). Cells are colored based on their $p_{0,i}$ values (higher $p_{0,i}$ is darker). Edge tensions are shown in red, with thickness proportional to tension. Both snapshots have the same distribution of target shape factors $\{p_{0,i}\}$.

units of length. We then have

$$e = \sum_i^N [k_{a,i}(a_i - a_{0,i})^2 + k_{p,i}(p_i - p_{0,i})^2], \quad (1)$$

where $\langle k_{a,i} \rangle = 1$, $\langle a_{0,i} \rangle = 1$, and p_i , $p_{0,i}$ are the dimensionless actual and preferred shape indices. Eq. (1) has been well studied for the case where $k_{a,i}$, $a_{0,i}$, $k_{p,i}$ have delta-function distributions, and $p_{0,i}$ has a distribution of zero [16, 18, 19] or nonzero width [28]. Here, we study Eq. 1 using the open-source CellGPU code [29], promoting $k_{a,i}$, $a_{0,i}$, $k_{p,i}$ and $p_{0,i}$ to learning DOF. Initially, N cell centers are chosen from a uniform random distribution in a square box with length $L = \sqrt{N}$; vertices and edges are defined from a Voronoi tessellation of these points. The energy in Eq. (1) is minimized using the FIRE algorithm [30].

We investigate the impact of various sets of learning DOF separately; e.g., when $p_{0,i}$ are learning DOF, we initialize $p_{0,i}$ values from a Gaussian distribution with mean $\langle p_{0,i} \rangle$ and standard deviation σ , and set $k_{a,i} = k_{p,i} = a_{0,i} = 1$ for all cells. As in Hagh, et al. [31], we focus on the case where the learning cost function is simply the energy, or the physical cost function. Hagh

et al. have shown that in sphere packings, minimizing the energy with respect to both physical DOF (particle positions) and learning DOF (particle radii) allows the system to find very rare low-energy states [31], shifting the jamming transition. We minimize the energy (Eq. (1)) with respect to both physical DOF (vertex positions) and learning DOF to study the influence of learning DOF on the rigidity transition. We keep the learning DOF distributions approximately fixed by imposing constraints on sets of moments of the distribution, such as the $m = \{-1, -2, -3, 1, 2, 3\}$ moments (see the SI). We also perform zero-temperature swap minimization to fix the distribution exactly. In this method, each of the N cells maintains its preferred property (introducing N constraints), cells are swapped in a trial move, and moves that lower the energy are accepted (see SI).

As the preferred shape index p_0 increases, confluent tissues with only physical degrees of freedom experience a solid-fluid phase transition at a critical value p_0^* [18, 32]. For systems with polydisperse $p_{0,i}$, the critical point p_0^* shifts towards larger average preferred shape factors with increasing standard deviation σ of the p_0 distribution [28] (black data in Fig. 3a). For a system with $p_{0,i}$ drawn from a Gaussian distribution with $\sigma = 0.2$ [22], we find $p_0^* = 4.05 \pm 0.02$ (curve with black circles in Fig. 1a). We evaluate rigidity based on the shear modulus G [33]: $G > 0$ in the rigid phase and $G = 0$ in the fluid phase. To compute G we freeze all learning DOF (see SI). Unless otherwise stated, error bars show the standard deviation over 50 samples. As $p_0 \rightarrow p_0^{*-}$, approaching the transition from the rigid side, the shear modulus vanishes as a power law: $G \approx a(p_0^* - p_0)^b$ with $b = 1.0$ [18, 32]. We subtract a finite-size-effect offset (see SI) and fit to this form to see how the scaling exponent b and the position of the rigidity transition, p_0^* , change as we introduce different sets of learning DOF.

Rigidity is associated with percolation of edges (cell-cell junctions) with nonzero tensions [28]. The tension of edge ij separating cells i and j is $T_{ij} = 2K_{P,i}(P_i - P_{0,i}) + 2K_{P,j}(P_j - P_{0,j})$, which when nondimensionalized becomes:

$$t_{ij} = 2k_{p,i}\sqrt{a_{0,i}}\tau_i^p + 2k_{p,j}\sqrt{a_{0,j}}\tau_j^p, \quad (2)$$

where $\tau_i^p = p_i - p_{0,i}$ is the tension of cell i in units of $\langle K_{A,i} \rangle \langle A_{0,i} \rangle^{3/2}$, i.e., energy/length. For $p_0 < p_0^*$, a percolating cluster of nonzero edge tensions (Fig. 1) maintains mechanical rigidity of tissue [28]. For $p_0 > p_0^*$, nonzero edge tensions fail to percolate and the tissue is fluid – it cannot resist shear deformation.

We first note that p_0^* is unaffected when the cell perimeter stiffnesses $\{k_{p,i}\}$ in Eq. 1 are allowed as learning DOF (Fig. 2). Clearly, manipulating $k_{p,i}$ cannot affect percolation of nonzero edge tensions if all the $k_{p,i}$ are positive. Therefore, allowing $k_{p,i}$ as learning DOF does not affect the rigidity transition. The scaling exponent b also remains unchanged but the tissue softens (see SI).

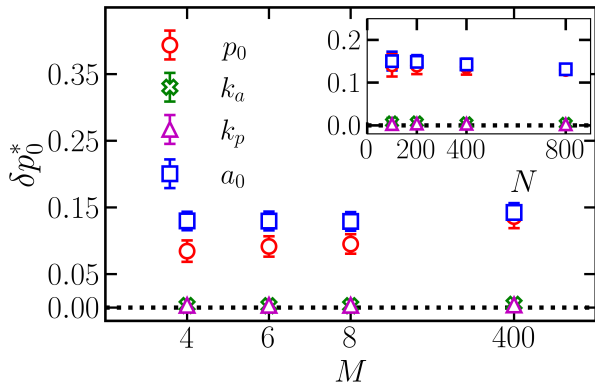


FIG. 2. Change in the rigidity transition point δp_0^* after introducing different transient degrees of freedom (different symbols), as a function of the number of constraints M on the distribution. Inset shows how δp_0^* varies with N for $M = 400$. The zero-temperature swap system is indicated by 400 constraints, the number of cells in the tissue. These results correspond to a standard deviation of $\sigma = 0.2$ of transient DOF.

We next consider variations in cell area stiffnesses $k_{a,i}$ as learning DOF with $a_{0,i} = 1$, $k_{p,i} = 1$ and $p_{0,i} = p_0$ for every cell i . One might expect the system to distribute its cell areas a_i to be closer to $a_{0,i} = 1$ for cells with larger values of $k_{a,i}$, leading to correlations that shift the transition. However, vertex models are unstressed at the rigidity transition [34], so their properties there cannot depend on $k_{a,i}$. As a result, the rigidity transition is unaffected by introducing $k_{a,i}$ as learning DOF.

We now consider preferred shape indices $\{p_{0,i}\}$ as learning DOF. Upon minimization, tissues adjust the values of some individual preferred shape indices $p_{0,i}$ to lower the energy by eliminating $p_i - p_{0,i}$. This leads to a lower fraction of nonzero tension edges, shifting the rigidity transition p_0^* to lower values (red triangles in Fig. 1a). Thus, minimizing E with respect to $p_{0,i}$ as well as the vertex positions introduces spatial correlations in $p_{0,i}$ that fluidize a tissue that would otherwise be solid. This shift persists whether we constrain certain moments of the p_0 -distribution or preserve the distribution exactly (see Fig. 2). The scaling exponent b for the shear modulus remains unaffected within our error bars (see SI). Moreover, the amplitude a of the shear modulus decreases more than when $k_{p,i}$ or $k_{a,i}$ are learning DOF (see SI).

Allowing $p_{0,i}$ as learning DOF not only shifts p_0^* but also increases the amount of structural order in the tissue (see SI). The hexatic order parameter [35] increases due to patches of high hexatic ordering. Interestingly, the local hexatic order of cell i shows a positive correlation with $p_i - p_{0,i}$. Evidently such order discourages percolation of tensional edges, shifting p_0^* downwards (see SI).

So far, we have used a fixed standard deviation ($\sigma = 0.2$) for the distribution of $\{p_{0,i}\}$. However, σ signif-

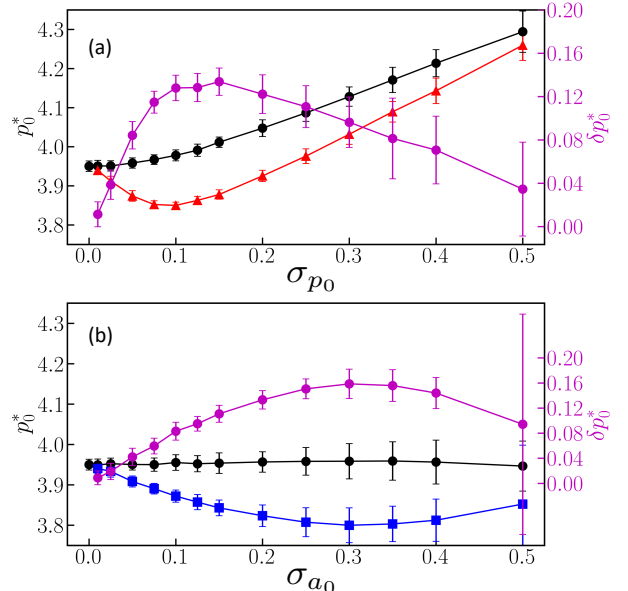


FIG. 3. The effect of polydispersity of learning DOF distributions on the rigidity transition point. (a) The left axis shows the transition point p_0^* versus the standard deviation σ_{p_0} of the $\{p_{0,i}\}$ distribution. When only vertex positions can vary during energy minimization (black circles), p_0^* increases with σ_{p_0} . However, when $\{p_{0,i}\}$ are also allowed to vary (red triangles), the behavior of p_0^* versus σ_{p_0} becomes non-monotonic. The right axis δp_0^* shows the reduction of p_0^* due to adding $\{p_{0,i}\}$ as degrees of freedom. (b) Same as (a), but with $\{a_{0,i}\}$ allowed to vary instead of $\{p_{0,i}\}$.

icantly influences tissue rigidity [28], shifting p_0^* upwards [28] (black circles in Fig. 3a). This raises the question: how does the shift in the transition p_0^* due to adding $p_{0,i}$ as learning DOF vary with σ ? We observe a reduction in p_0^* at all σ (compare the red triangles to black circles in Fig. 3a). Interestingly, the magnitude of this reduction is non-monotonic. The purple curve in Fig. 3a, δp_0^* , shows that the shift in the transition is maximal at $\sigma \approx 0.15$. This suggests there is an optimal level of cell-to-cell fluctuations in biological tissues that enables learning to modulate rigidity.

To understand this non-monotonicity, we first note that as σ approaches zero, the $\{p_{0,i}\}$ distribution approaches a delta-function and no learning is possible. Therefore, δp_0^* must increase away from that point. To understand why δp_0^* decreases for $\sigma \gtrsim 0.15$, we analyzed the correlations between p and p_0 across all cells, both with and without p_0 as learning DOF. As expected, the Pearson's correlation coefficient $\rho(p, p_0)$ rises when we incorporate cell p_0 values as learning DOF across all σ values (see SI); the energy is lowered by bringing p_i closer to $p_{0,i}$. But for $\sigma \gtrsim 0.15$, p and p_0 already exhibit strong correlations even when $p_{0,i}$ are not learning DOF. Introducing $p_{0,i}$ as learning DOF only marginally enhances this correlation, so δp_0^* decreases as shown in Fig. 3.

Finally, we consider the preferred cell areas, $A_{0,i}$. In tissues where $A_{0,i} = A_0$ is the same for all cells, altering A_0 while keeping P_0 fixed does not affect p_0^* due to the confluence constraint ($\sum A_i = \text{constant} = L^2$) [36, 37]. Yang et al. [36] found that the difference between A_0 and the actual area $\langle A \rangle = N/L^2$ alters the overall pressure of the system, but not the shear stresses. We find that even in the presence of heterogeneous $A_{0,i}$ values, p_0^* is unaffected by changes in the *average* target area $\langle A_0 \rangle$ (see SI), so in what follows we hold $\langle A_0 \rangle = 1$ fixed. The solid black circles in Fig. 3b shows that varying the *width* of the distribution of the dimensionless $a_{0,i}$ in Eq. 1 also does not affect the transition point. Note that defining target shape factors as $P_{0,i}/\langle A_i \rangle$ would introduce variability in the transition point with σ_{a_0} (see SI). This suggests that the enhanced rigidity discussed in Ref. [28] is caused by heterogeneity in target shape indices ($p_{0,i} = P_{0,i}/\sqrt{A_{0,i}}$) and not by heterogeneity in $P_{0,i}$.

Given these results, we promote $\{A_{0,i}\}$ to learning DOF while keeping $\langle A_{0,i} \rangle$ fixed. This introduces *two* sets of learning DOF in the dimensionless energy in Eq. 1, namely $\{a_{0,i}\}$ and $\{p_{0,i}\}$. We have already shown how introducing $\{p_{0,i}\}$ as learning DOF affects rigidity, so now we consider the effects of $a_{0,i}$ in isolation. To do so, we maintain a constant target shape factor for cells, i.e., $p_{0,i} = p_0$, by coupling the target perimeters $\{P_{0,i}\}$ with the target areas: $\{P_{0,i} = p_0\sqrt{A_{0,i}}\}$. This allows us to consider only $\{a_{0,i}\}$ while keeping the average $\langle A_{0,i} \rangle = 1.0$ at homogeneous $p_{0,i} = p_0$. We find that introducing $\{a_{0,i}\}$ as learning DOF leaves the scaling exponent for the shear modulus unchanged (see SI). Similar to $\{p_{0,i}\}$, the $\{a_{0,i}\}$ learning DOF shift the transition downwards. This occurs at all values of the width of $\{a_{0,i}\}$ distribution, σ_{a_0} , with the maximum shift occurring around $\sigma_{a_0} \approx 0.3$. Correlations in $a_{0,i}$ from cell to cell causes τ_{ij} in Eq. 2 to vanish for some edges, shifting the percolation of nonzero tensions to lower p_0^* .

We have explored the effects of adding learning degrees of freedom in 2D vertex models on the rigidity transition, p_0^* . The transition is unaffected when cell stiffnesses K_A and K_P are allowed to vary. In contrast, introducing preferred cell areas or perimeters as learning degrees of freedom significantly alters the tissue's energy landscape, shifting p_0^* downwards. Learned spatial correlations in p_0 or a_0 can fluidize a tissue, and there are optimal values for the heterogeneity in p_0 ($\sigma_{p_0} \approx 0.15$) and a_0 ($\sigma_{a_0} \approx 0.3$) that lead to the largest shift of the transition.

Learning DOF have previously been introduced into networks that become rigid when the number of physical degrees of freedom equals the number of physical constraints [2–4, 31]. In contrast, vertex models are highly under-constrained and become rigid through geometric incompatibility [34]. Our finding that rigidity in these models is also strongly affected by learning DOF suggests that vertex models can learn.

It is well-established that systems with fixed topology

can learn intricate tasks [6]. While Hagh et al. [31] demonstrated that jammed particle packings subject to frequent rearrangements can learn to identify ultra stable states, it is difficult to tune arbitrary mechanical responses into *typical* jammed states because they are marginally stable to rearrangements [38]. Confluent epithelial tissues lie in an intermediate state between these two extremes – topological rearrangements, primarily in the form of T1 transitions, can occur but are not nearly as prevalent as in jammed packings. Our finding that preferred shape indices and cell areas effectively tune rigidity in vertex models suggests that introducing them as learning DOF could be a fruitful way of obtaining complex responses in systems that allow topological rearrangements.

The framework of physical learning with $\{p_{0,i}\}$ or $\{a_{0,i}\}$ as learning DOF could provide a new paradigm for understanding biological tissue mechanics. Individual cells can control cell- and molecular-scale properties, including the concentration of adhesion molecules and myosin motors, which in turn govern the preferred shape index locally [22, 39]. Our work indicates that tissues should be able to learn if they follow a global gradient closely enough. In other systems, it has been possible to identify local learning rules that project sufficiently onto the global gradient to allow learning [7–9, 11, 12]. It would be interesting to study whether local rules governing the dynamics of cell shapes and tensions that have already been proposed [23, 40, 41] project onto gradients of useful global learning cost functions, or conversely, to hypothesize learning cost functions for tissues and search for possible local learning rules that enable them to be minimized. More broadly, this framework could be useful for predicting how the dynamics of tissues arises from variation of cellular properties across developmental or evolutionary timescales.

Acknowledgements — We thank Varda F. Hagh, R. Cameron Dennis, and Elizabeth Lawson-Keister for helpful discussions. MLM and SA were supported by Simons Foundation #454947, NSF-DMR-1951921 and SU's Orange Grid research computing cluster. IT was supported by the National Science Foundation through DMR-2005749 and AJL by the Simons Foundation #327939. AJL thanks CCB at the Flatiron Institute, a division of the Simons Foundation, and the Isaac Newton Institute for Mathematical Sciences at Cambridge University (EPSRC grant EP/R014601/1), for support and hospitality.

-
- [1] Jason W. Rocks, Nidhi Pashine, Irmgard Bischofberger, Carl P. Goodrich, Andrea J. Liu, and Sidney R. Nagel. Designing allosteric-inspired response in mechanical networks. *Proceedings of the National Academy of Sciences*, 114(10):2520–2525, March 2017. Publisher: Proceedings of the National Academy of Sciences.

- [2] Carl P. Goodrich, Andrea J. Liu, and Sidney R. Nagel. The Principle of Independent Bond-Level Response: Tuning by Pruning to Exploit Disorder for Global Behavior. *Physical Review Letters*, 114(22):225501, June 2015. Publisher: American Physical Society.
- [3] Daniel Hexner, Andrea J. Liu, and Sidney R. Nagel. Role of local response in manipulating the elastic properties of disordered solids by bond removal. *Soft Matter*, 14(2):312–318, 2018.
- [4] Daniel Hexner, Andrea J. Liu, and Sidney R. Nagel. Linking microscopic and macroscopic response in disordered solids. *Physical Review E*, 97(6):063001, June 2018.
- [5] Jason W. Rocks, Henrik Ronellenfitsch, Andrea J. Liu, Sidney R. Nagel, and Eleni Katifori. Limits of multifunctionality in tunable networks. *Proceedings of the National Academy of Sciences*, 116(7):2506–2511, February 2019. Publisher: Proceedings of the National Academy of Sciences.
- [6] Menachem Stern and Arvind Murugan. Learning Without Neurons in Physical Systems. *Annual Review of Condensed Matter Physics*, 14(1):417–441, 2023. eprint: <https://doi.org/10.1146/annurev-conmatphys-040821-113439>.
- [7] Nidhi Pashine, Daniel Hexner, Andrea J. Liu, and Sidney R. Nagel. Directed aging, memory, and nature’s greed. *Science Advances*, 5(12):eaax4215, December 2019. Publisher: American Association for the Advancement of Science.
- [8] Daniel Hexner, Nidhi Pashine, Andrea J. Liu, and Sidney R. Nagel. Effect of directed aging on nonlinear elasticity and memory formation in a material. *Physical Review Research*, 2(4):043231, November 2020. Publisher: American Physical Society.
- [9] Daniel Hexner, Andrea J. Liu, and Sidney R. Nagel. Periodic training of creeping solids. *Proceedings of the National Academy of Sciences*, 117(50):31690–31695, December 2020. Publisher: Proceedings of the National Academy of Sciences.
- [10] Benjamin Scellier and Yoshua Bengio. Equilibrium Propagation: Bridging the Gap between Energy-Based Models and Backpropagation. *Frontiers in Computational Neuroscience*, 11, 2017.
- [11] Menachem Stern, Daniel Hexner, Jason W. Rocks, and Andrea J. Liu. Supervised Learning in Physical Networks: From Machine Learning to Learning Machines. *Physical Review X*, 11(2):021045, May 2021. Publisher: American Physical Society.
- [12] Sam Dillavou, Menachem Stern, Andrea J. Liu, and Douglas J. Durian. Demonstration of Decentralized Physics-Driven Learning. *Physical Review Applied*, 18(1):014040, July 2022. Publisher: American Physical Society.
- [13] J. F. Wycoff, S. Dillavou, M. Stern, A. J. Liu, and D. J. Durian. Desynchronous learning in a physics-driven learning network. *The Journal of Chemical Physics*, 156(14):144903, April 2022.
- [14] Sam Dillavou, Benjamin D. Beyer, Menachem Stern, Marc Z. Miskin, Andrea J. Liu, and Douglas J. Durian. Machine Learning Without a Processor: Emergent Learning in a Nonlinear Electronic Metamaterial, November 2023. arXiv:2311.00537 [cond-mat].
- [15] Lars Hufnagel, Aurelio A. Teleman, Hervé Rouault, Stephen M. Cohen, and Boris I. Shraiman. On the mechanism of wing size determination in fly development. *Proceedings of the National Academy of Sciences*, 104(10):3835–3840, March 2007. Publisher: Proceedings of the National Academy of Sciences.
- [16] Reza Farhadifar, Jens-Christian Röper, Benoit Aigouy, Suzanne Eaton, and Frank Jülicher. The Influence of Cell Mechanics, Cell-Cell Interactions, and Proliferation on Epithelial Packing. *Current Biology*, 17(24):2095–2104, December 2007.
- [17] Jin-Ah Park, Jae Hun Kim, Dapeng Bi, Jennifer A. Mitchel, Nader Taheri Qazvini, Kelan Tantisira, Chan Young Park, Maureen McGill, Sae-Hoon Kim, Bomi Gweon, Jacob Notbohm, Robert Steward Jr, Stephanie Burger, Scott H. Randell, Alvin T. Kho, Dhananjay T. Tambe, Corey Hardin, Stephanie A. Shore, Elliot Israel, David A. Weitz, Daniel J. Tschumperlin, Elizabeth P. Henske, Scott T. Weiss, M. Lisa Manning, James P. Butler, Jeffrey M. Drazen, and Jeffrey J. Fredberg. Unjamming and cell shape in the asthmatic airway epithelium. *Nature Materials*, 14(10):1040–1048, October 2015. Number: 10 Publisher: Nature Publishing Group.
- [18] Dapeng Bi, J. H. Lopez, J. M. Schwarz, and M. Lisa Manning. A density-independent rigidity transition in biological tissues. *Nature Physics*, 11(12):1074–1079, December 2015. Number: 12 Publisher: Nature Publishing Group.
- [19] Dapeng Bi, Xingbo Yang, M. Cristina Marchetti, and M. Lisa Manning. Motility-Driven Glass and Jamming Transitions in Biological Tissues. *Physical Review X*, 6(2):021011, April 2016. Publisher: American Physical Society.
- [20] M. Chiang and D. Marenduzzo. Glass transitions in the cellular Potts model. *Europhysics Letters*, 116(2):28009, December 2016. Publisher: EDP Sciences, IOP Publishing and Società Italiana di Fisica.
- [21] Alessandro Mongera, Payam Rowghanian, Hannah J. Gustafson, Elijah Shelton, David A. Kealhofer, Emmet K. Carn, Friedhelm Serwane, Adam A. Lucio, James Giandomma, and Otger Campàs. A fluid-to-solid jamming transition underlies vertebrate body axis elongation. *Nature*, 561(7723):401–405, September 2018.
- [22] Xun Wang, Matthias Merkel, Leo B. Sutter, Gonca Erdemci-Tandogan, M. Lisa Manning, and Karen E. Kasza. Anisotropy links cell shapes to tissue flow during convergent extension. *Proceedings of the National Academy of Sciences*, 117(24):13541–13551, June 2020. Publisher: National Academy of Sciences Section: Biological Sciences.
- [23] Nikolas H. Claussen, Fridtjof Brauns, and Boris I. Shraiman. A Geometric Tension Dynamics Model of Epithelial Convergent Extension, November 2023. arXiv:2311.16384 [cond-mat, physics:physics, q-bio].
- [24] Gonca Erdemci-Tandogan, Madeline J. Clark, Jeffrey D. Amack, and M. Lisa Manning. Tissue Flow Induces Cell Shape Changes During Organogenesis. *Biophysical Journal*, 115(11):2259–2270, December 2018.
- [25] Paula C. Sanematsu, Gonca Erdemci-Tandogan, Himani Patel, Emma M. Retzlaff, Jeffrey D. Amack, and M. Lisa Manning. 3D viscoelastic drag forces contribute to cell shape changes during organogenesis in the zebrafish embryo. *Cells & Development*, 168:203718, December 2021.
- [26] Indrajit Tah, Daniel Haertter, Janice M. Crawford, Daniel P. Kiehart, Christoph F. Schmidt, and Andrea J. Liu. Minimal vertex model explains how the amnioserosa avoids fluidization during *Drosophila* dorsal closure, December 2023. arXiv:2312.12926 [physics, q-bio].

- [27] Hisao Honda. Description of cellular patterns by Dirichlet domains: The two-dimensional case. *Journal of Theoretical Biology*, 72(3):523–543, June 1978.
- [28] Xinzhi Li, Amit Das, and Dapeng Bi. Mechanical Heterogeneity in Tissues Promotes Rigidity and Controls Cellular Invasion. *Physical Review Letters*, 123(5):058101, July 2019.
- [29] Daniel M. Sussman. cellGPU: Massively parallel simulations of dynamic vertex models. *Computer Physics Communications*, 219:400–406, October 2017.
- [30] Erik Bitzek, Pekka Koskinen, Franz Gähler, Michael Moseler, and Peter Gumbsch. Structural Relaxation Made Simple. *Physical Review Letters*, 97(17):170201, October 2006.
- [31] Varda F. Hagh, Sidney R. Nagel, Andrea J. Liu, M. Lisa Manning, and Eric I. Corwin. Transient learning degrees of freedom for introducing function in materials. *Proceedings of the National Academy of Sciences*, 119(19):e2117622119, May 2022. Publisher: Proceedings of the National Academy of Sciences.
- [32] Matthias Merkel, Karsten Baumgarten, Brian P. Tighe, and M. Lisa Manning. A minimal-length approach unifies rigidity in underconstrained materials. *Proceedings of the National Academy of Sciences*, 116(14):6560–6568, April 2019.
- [33] Matthias Merkel and M Lisa Manning. A geometrically controlled rigidity transition in a model for confluent 3D tissues. *New Journal of Physics*, 20(2):022002, February 2018.
- [34] Ojan Khatib Damavandi, Varda F. Hagh, Christian D. Santangelo, and M. Lisa Manning. Energetic rigidity. I. A unifying theory of mechanical stability. *Physical Review E*, 105(2):025003, February 2022.
- [35] Paul J Steinhardt, David R Nelson, and Marco Ronchetti. Bond-orientational order in liquids and glasses. *Physical Review B*, 28(2):784, 1983.
- [36] Xingbo Yang, Dapeng Bi, Michael Czajkowski, Matthias Merkel, M. Lisa Manning, and M. Cristina Marchetti. Correlating cell shape and cellular stress in motile confluent tissues. *Proceedings of the National Academy of Sciences*, 114(48):12663–12668, November 2017. Publisher: National Academy of Sciences Section: Physical Sciences.
- [37] Eyal Teomy, David A. Kessler, and Herbert Levine. Confluent and nonconfluent phases in a model of cell tissue. *Physical Review E*, 98(4):042418, October 2018. Publisher: American Physical Society.
- [38] B. Pisanty. (private communication, 2023).
- [39] Preeti Sahu, Daniel M. Sussman, Matthias Rübsam, Aaron F. Mertz, Valerie Horsley, Eric R. Dufresne, Carien M. Niessen, M. Cristina Marchetti, M. Lisa Manning, and J. M. Schwarz. Small-scale demixing in confluent biological tissues. *Soft Matter*, 16(13):3325–3337, 2020. Publisher: Royal Society of Chemistry.
- [40] Michael F. Staddon, Kate E. Cavannaugh, Edwin M. Munro, Margaret L. Gardel, and Shiladitya Banerjee. Mechanosensitive Junction Remodeling Promotes Robust Epithelial Morphogenesis. *Biophysical Journal*, 117(9):1739–1750, November 2019.
- [41] Nicholas Noll, Madhav Mani, Idse Heemskerk, Sebastian J. Streichan, and Boris I. Shraiman. Active tension network model suggests an exotic mechanical state realized in epithelial tissues. *Nature Physics*, 13(12):1221–1226, December 2017.

SUPPLEMENTAL INFORMATION

Details of the model

In these coarse-grained vertex models, tissue monolayers are described as a network of polygonal cells and the physical degrees of freedom (DOF) are the vertices of these polygons. Cellular properties and interactions are encoded in an energy function

$$E = \sum_i^N [K_{A,i}(A_i - A_{0,i})^2 + K_{P,i}P_i^2 + \gamma_i P_i], \quad (\text{S1})$$

where A_i and $A_{0,i}$ are the current and preferred cell areas, P_i is the cell perimeter, γ_i is the interfacial tension, and $K_{A,i}$, $K_{P,i}$ are the area and perimeter stiffnesses, respectively. The first term in energy is due to monolayer's resistance to height fluctuations and cells incompressibility. The active contractility of actomyosin cortex is captured as a quadratic penalty in cell perimeters in the second term of Eq. (S1). The competition between cortical tension and cell-cell adhesion of contacting cells results in an interfacial tension γ_i that is included in the last term.

By adding a constant term $P_{0,i} = -\gamma_i/(2K_{P,i})$ —a preferred perimeter—to Eq. (S1), we obtain

$$E = \sum_i^N [K_{A,i}(A_i - A_{i0})^2 + K_{P,i}(P_i - P_{i0})^2]. \quad (\text{S2})$$

Using the energy scale $\langle K_{A,i} \rangle \langle A_{0,i} \rangle^2$ and the length scale $\sqrt{\langle A_{0,i} \rangle}$, we can non-dimensionalize this elastic energy as

$$e = \sum_i^N [k_{a,i}(a_i - a_{0,i})^2 + k_{p,i}(p_i - p_{0,i})^2]. \quad (\text{S3})$$

Details of energy minimization

To simulate a 2D vertex model, we use the CellGPU open-source code [29]. We randomly generate cell positions in a periodic square box of lateral length $L = \sqrt{N}$, where N is the number of cells. We create the initial tissue by Voronoi tessellation of these points. In order to analyze the mechanical behavior of biological tissues at zero temperature, we minimize the elastic energy in Eq. (S3) using FIRE [30]. Once we achieve the minimum energy state, we calculate properties such as linear shear modulus G to determine the mechanical stability of our system. Below, we briefly explain how to compute forces in a vertex model as well as how to perform energy minimization with various degrees of freedom.

Minimizing e with respect to physical degrees of freedom

The individual cell areas and perimeters are calculated from positions of vertices $\{\vec{r}_m\}$ associated with that cell. For a cell i with n vertices (or number of neighbors), we have

$$\begin{aligned} P_i &= \sum_{m=1}^n \|\vec{r}_{m+1} - \vec{r}_m\| \\ A_i &= \frac{1}{2} \sum_{m=1}^n (\vec{r}_{m+1,x} + \vec{r}_{m,x})(\vec{r}_{m+1,y} - \vec{r}_{m,y}) \end{aligned} \quad (\text{S4})$$

where the summation goes counterclockwise around vertices of the cell and we define $\vec{r}_{n+1} = \vec{r}_1$. For finding the area of a polygon, we use the trapezoid formula. However, other formulas like the shoelace or triangle formulas can also be used. The total force on vertex m is computed by adding the force contribution of its three adjacent cells. The α component of the force contribution of cell i on vertex m is

$$\begin{aligned} f_{m,\alpha}^i &= -\frac{\partial e_i}{\partial r_{m,\alpha}} = -2k_{a,i}(a_i - a_{0,i})\frac{\partial a_i}{\partial r_{m,\alpha}} \\ &\quad - 2k_{p,i}(p_i - p_{0,i})\frac{\partial p_i}{\partial r_{m,\alpha}}, \end{aligned} \quad (\text{S5})$$

where the derivatives of area and perimeter are computed from calculating the derivatives of Eq. (S4). After finding the α component of force contributions of three cells that vertex m is part of, we obtain the total force $f_{m,\alpha} = \sum_{i=1,2,3} f_{m,\alpha}^i$. In order to find the minimum energy configuration, we use FIRE [30]. The minimization algorithm is stopped when $\max(\|f_m\|)/N_v$, where N_v is the number of degrees of freedom (here the number of vertices), becomes less than 10^{-10} . During energy minimization, the network topology is updated using T1 transitions with an edge threshold of 10^{-5} .

Minimizing e with respect to both physical and learning degrees of freedom

The internal degrees of freedom like $\{k_{p,i}\}$ and $\{p_{0,i}\}$ can be added in the minimization procedure to study the effects of these additional DOF on the mechanics of tissue. We study the effect of these different types of learning DOF one at a time. For example, when adding target shape factors $\{p_{0,i}\}$, we set $k_{a,i} = a_{0,i} = k_{p,i} = 1$ for all cells. We initialize $p_{0,i}$ values from a Gaussian distribution with a standard deviation of σ and mean $\langle p_{0,i} \rangle$. These $\{p_{0,i}\}$ are basically added in the minimization procedure similar to the physical DOF. The forces on these new DOF are computed as

$$f_{p_{0,i}} = -\frac{\partial e_i}{\partial p_{0,i}} = 2k_{p,i}(p_i - p_{0,i}). \quad (\text{S6})$$

The energy in Eq. (S3) is then minimized with respect to both vertex positions (physical DOF) and these $\{p_{0,i}\}$ (learning DOF). We note that the convergence of the minimization algorithm is more robust if we first minimize the physical DOF before including these additional DOF. In the case of $\{p_{0,i}\}$ DOF, if there are no constraints on the distribution of $\{p_{0,i}\}$, the system tunes these new DOF until $p_i - p_{0,i} = 0$, which results in a fluid state at the mean shape index of $\langle p_{0,i} \rangle \simeq 4.1$. In the case of $\{k_{p,i}\}$ DOF, without any constraints on the distribution of these new DOF, cells can arbitrary lower their $k_{p,i}$ during energy minimization.

To avoid these pathological states, we fix the distribution of learning DOF by constraining a set of moments, e.g., when adding $\{p_{0,i}\}$ as new DOF, we fix $\phi_k = \sum_i p_{0,i}^k$ where $k = \{m_1, m_2, \dots, m_n\}$, m_i is an integer value. With a sufficient number of moments, we find that the $\{p_{0,i}\}$ distribution is preserved during our energy minimization within an error margin. In presence of these constraints, the forces $f_{p_{0,i}}$ are modified in the constrained space of these moments. After finding the constraint Jacobian \mathbf{J} of these moments as

$$\mathbf{J}_{k,i} = \frac{\partial \phi_k}{\partial p_{0,i}} = kp_{0,i}^{k-1}. \quad (\text{S7})$$

The orthonormalized constraint basis \mathbf{J}_o can be computed using the Gram–Schmidt process. Therefore, the forces on $p_{0,i}$ in Eq. (S6) are projected in this constrained space [31]

$$f_{p_{0,i}}^c = f_{p_{0,i}} - \mathbf{J}_o \mathbf{J}_o^T f_{p_{0,i}} \quad (\text{S8})$$

By using these constrained forces $f_{p_{0,i}}^c$, we ensure that the system does not alter the moments ϕ_k . Above, we explained the simulation procedure for adding $\{p_{0,i}\}$ as learning DOF. Adding other types of learning DOF like $\{k_{p,i}\}$ is done in a similar way. We observe that when constrained minimization is applied to learning degrees of freedom, there is a possibility that the system may not maintain the distribution within our desired error margin, particularly near the transition point. This happens even though all specified moments are preserved. To overcome this limitation, we have also employed a zero-temperature swap minimization technique. This approach precisely maintains the distribution of the learning degrees of freedom. We describe this minimization method in the subsequent section.

Zero-temperature swap minimization method

A useful limit of adding learning DOF is when the distribution of the learning DOF is exactly fixed. For instance, in the case of $p_{0,i}$ DOF, we start by drawing the target shape factors of cells from a Gaussian distribution with a standard deviation of σ and an average $\langle p_{0,i} \rangle$. To

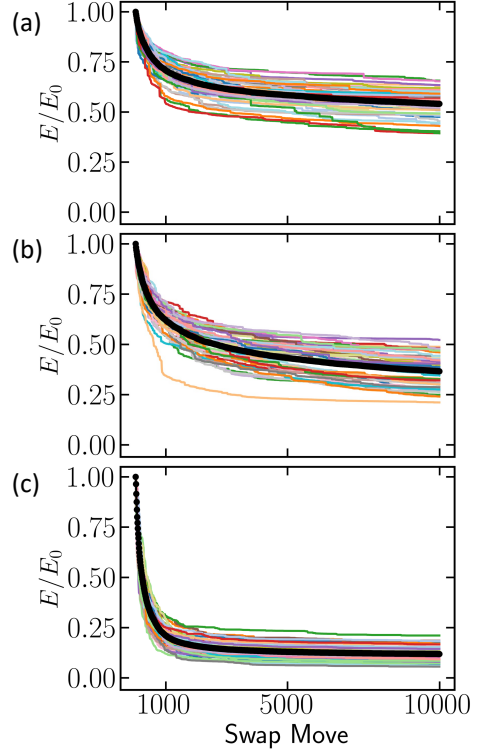


FIG. S1. Energy ratio versus zero-temperature swap moves when the target shape factors of cells $\{p_{0,i}\}$ are drawn from a normal distribution with a standard deviation $\sigma = 0.2$. (a) For an average target shape factor of $\langle p_{0,i} \rangle = 3.7$ (b) For an average target shape factor of $\langle p_{0,i} \rangle = 3.75$ (c) For an average target shape factor of $\langle p_{0,i} \rangle = 3.9$. The dark markers show the mean value and the thin lines show 50 different samples. We used $N = 300$ cells in our simulations.

make sure that the distribution of $p_{0,i}$ is exactly fixed, we randomly swap $p_{0,i}$ of two cells, minimize the energy with respect to the vertex positions, and accept the swap move only if the energy decreases, illustrated by the following pseudocode:

```

 $e_1 =$  Minimized energy wrt vertex positions
Swap cells i and j
 $e_2 =$  Minimized energy wrt vertex positions
if  $e_2 < e_1$  then
    Accept this swap move
else
    Reject this swap move
end if

```

Figure S1 shows the energy versus number of these zero-temperature swap moves at different values of the average target shape factor. The energy continuously decreases as a function of swap moves until it reaches a plateau. For system sizes studied, we find that typically $\sim 10^4$ swap moves results in a plateau.

Shear modulus calculation

As a measure for rigidity, we focus on the linear shear modulus G of the vertex model. It is important to note that while energy minimization might include learning degrees of freedom (DOF), these additional DOF are frozen during the calculation of G . Essentially, learning DOF are utilized solely to attain new configurations of the tissue. The solid-like state of the tissue is characterized by a finite value of G , whereas in a fluid-like state, G is zero. The shear modulus is determined by computing the second derivative of the system's energy in relation to an infinitesimally small applied simple shear strain γ

$$G = \frac{1}{L^2} \frac{\partial^2 E}{\partial \gamma^2}, \quad (\text{S9})$$

where $L = \sqrt{N_c}$ is the lateral dimension of the simulation box. Rather than applying multiple strain deformations and numerically calculating this second derivative, the shear modulus can be efficiently determined from the Hessian matrix corresponding to the energy-minimized state [33]. The elements of the Hessian are constituted by the second derivatives of the energy in relation to the positions of the vertices

$$D_{i\alpha,j\beta} = \frac{\partial^2 E}{\partial r_{i\alpha} \partial r_{j\beta}}, \quad (\text{S10})$$

where $r_{i\alpha}$ and $r_{j\beta}$ are the α component of the coordinates of vertex i and β component of the coordinates of vertex j , respectively. It can be shown that [33]

$$G = \frac{1}{L^2} \left(\frac{\partial^2 E}{\partial \gamma^2} - \sum_m \frac{1}{\omega_m^2} \left[\sum_{j,\alpha} \frac{\partial^2 E}{\partial \gamma \partial r_{j\alpha}} u_{j\alpha}^m \right]^2 \right), \quad (\text{S11})$$

where ω_m^2 are the non-zero eigenvalues of the Hessian matrix and $u_{j\alpha}^m$ are the corresponding normalized eigenvectors.

To analyze the scaling behavior of G as it approaches the critical point p_0^* , we employ a bisection method to differentiate between the rigid and floppy states of the tissue. We start with an initial bracket $[p_0^S, p_0^F]$, where $p_0^S = 3.65$ represents the solid state and $p_0^F = 4.2$ represents the fluid state. Subsequently, we iteratively narrow this bracket by conducting minimizations at its midpoint $p_0 = \frac{p_0^S + p_0^F}{2}$. We note that we do not include the box shear degrees of freedom in our minimization procedure. The criterion for adjusting the bracket is based on the shear modulus. Specifically, if the system has a shear modulus below a pre-defined threshold (in this case, 10^{-4}), the fluid boundary p_0^F is updated to the current midpoint p_0 . Conversely, if the shear modulus exceeds this threshold, the solid boundary p_0^S is updated in a similar manner. We perform at least 20 iterations of this

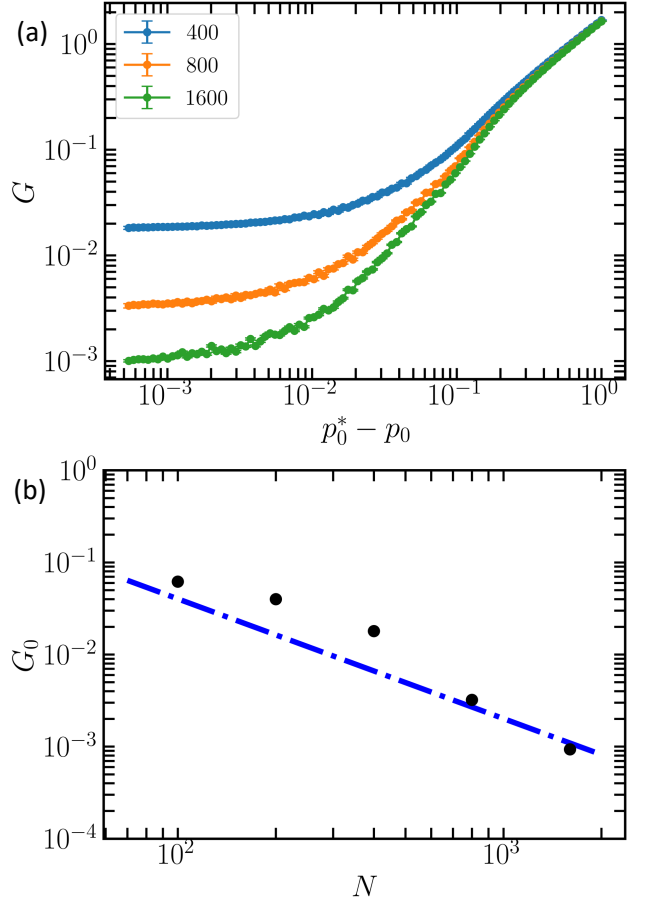


FIG. S2. The behavior of shear modulus G versus the distance to the critical point without shear-stabilization. (a) The shear modulus G versus the distance to the rigidity transition point that was obtained using bisections. (b) The onset of shear modulus G_0 at the critical point p_0^* , i.e., the plateau in (a), versus system size N . This plateau vanishes at large N (the dashed line shows a slope of -1.3). These results are for energy minimized-states with respect to only physical degrees of freedom. All cells here have the same p_0 values, i.e., there is no polydispersity in p_0 parameter.

bisection process to accurately locate the tissue's rigidity transition point.

Figure S2 illustrates the behavior of G versus its distance from the critical point for various system sizes. Notably, as we approach p_0^* , G exhibits a plateau that disappears in the thermodynamic limit. This observation aligns with previous work, indicating that such a plateau is absent in the shear-stabilized tissues [32].

Incorporating additional learning degrees of freedom leads to a decrease in tissue rigidity. Notably, introducing either $p_{0,i}$ or $a_{0,i}$ degrees of freedom leads to a more significant decrease in the shear modulus G compared to the effect of cell stiffness DOF. This is clearly shown in Figure S3. Interestingly, the scaling exponent of the shear modulus near the critical point remains unaffected as various learning DOFs are introduced, as demonstrated in

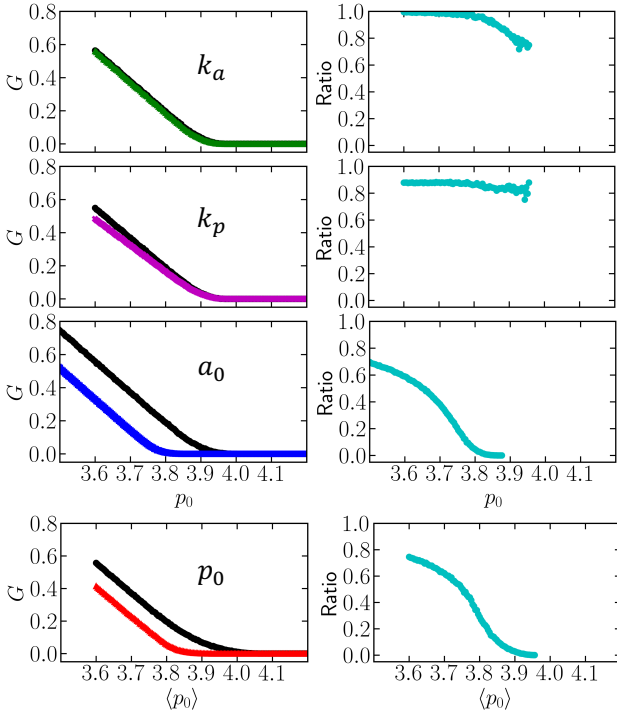


FIG. S3. The effect of adding various learning DOF in vertex models on the shear modulus G . Each plot specifies the type of newly added DOF. Dark markers indicate the behavior of G in the absence of any learning DOF. For these simulations, the standard deviation for the distributions of learning DOF is fixed at $\sigma = 0.2$. On the right side of each plot, we display the ratio of G values obtained with the inclusion of new DOF compared to those without.

Figure S4.

The effect of target area A_0

Yang et al.[36] have demonstrated that the manipulation of A_0 within a homogeneous system exhibits no impact on the mechanics of vertex models such as shear modulus and rigidity transition point. Here, we show that even in a heterogeneous system with polydispersity in A_0 , changing the average of A_0 distribution does not change the shear modulus behavior. Here, we assume that K_A , K_P , and P_0 are fixed and uniform for every cell.

$$\begin{aligned} E &= \sum_i K_A (A_i - A_{0i})^2 + K_P (P_i - P_0)^2 \quad (\text{S12}) \\ &= \sum_i K_A A_i^2 - 2K_A \sum_i A_i A_{0i} + \sum_i K_A A_{0i}^2 \\ &\quad + \sum_i K_P (P_i - P_0)^2 \end{aligned}$$

We can find the following by adding and subtracting the term $\frac{K_A}{N} A_t^2$ to the equation above, where $A_t = \sum_i A_i =$

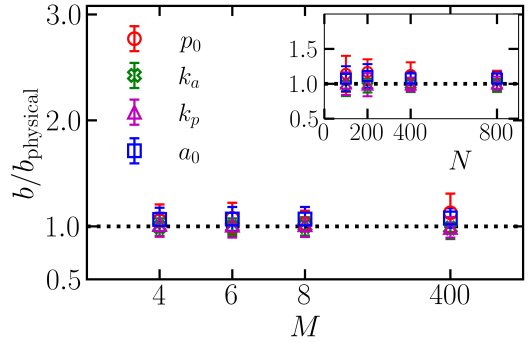


FIG. S4. The effect of transient degrees of freedom on the scaling exponent b of the shear modulus as a function of constraints on the distribution. The zero-temperature swap system is indicated by 400 constraints, the number of cells in the tissue. The results are for a standard deviation of $\sigma = 0.2$ of transient degrees of freedom.

L^2 represents the total tissue area

$$\begin{aligned} E &= \sum_i (A_i - \langle A \rangle)^2 + \frac{K_A}{N} A_t^2 - 2K_A \sum_i A_i A_{0i} \quad (\text{S13}) \\ &\quad + \sum_i K_A A_{0i}^2 + \sum_i K_P (P_i - P_0)^2 \end{aligned}$$

where $\langle A \rangle$ is the average area per cell, $\langle A \rangle = L^2/N$. Note that the terms $\frac{K_A}{N} A_t^2$ and $\sum_i K_A A_{0i}^2$ are constant offsets in the energy function. However, the term $2K_A \sum_i A_i A_{0i}$ can affect the forces on vertices. This term can be simplified by substituting $A_i = \langle A \rangle + \delta A_i$ and $A_{0i} = \langle A_0 \rangle + \delta A_{0i}$

$$\sum_i A_i A_{0i} = A_t \langle A_0 \rangle + \sum_i \delta A_i \delta A_{0i} \quad (\text{S14})$$

The first term in the equation above indicates that the average value of the A_{0i} distribution affects the overall pressure of the system by a factor of $2K_A \langle A_0 \rangle$. This effect is similar to that of a system where all cells have homogeneous A_{0i} values. The second term in the equation can cause the forces on vertices to change. This happens because there may be fluctuations in both the target area and the current area of the cell. We note that $\sum_i \delta A_i \delta A_{0i} = (N - 1) \text{Cov}(A, A_0)$. By analyzing our simulation data, we find that this term is negligible compared to other terms in the elastic energy. As a result, even in the context of a heterogeneous tissue with a polydisperse distribution in A_{0i} , variations in the target area A_0 exert no significant impact on the shear modulus. Consequently, when A_{0i} values are introduced as learning degrees of freedom in tissues, changing their average $\langle A_{0i} \rangle$, while maintaining constant and uniform target perimeters $P_{0,i}$, does not result in any alteration of the shear modulus behavior.

Importantly, changing the width σ_{a_0} of the $A_{0,i}$ distribution in systems *without learning DOF* also does not

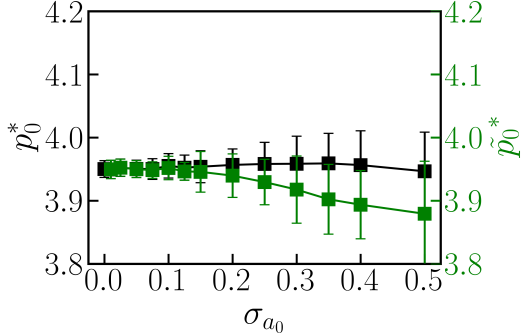


FIG. S5. Comparison of rigidity transition points using two definitions of the target shape factor. The energy minimization is performed solely with respect to physical degrees of freedom with a distribution of $a_{0,i}$ values at different standard deviations σ_{a_0} . Here, we define $a_{0,i}$ as $A_{0,i}/\langle A_{0,i} \rangle$, with $\langle A_{0,i} \rangle = 1$. In the simulations, we maintain a fixed target shape factor defined as $p_{0,i} = p_0 = P_{0,i}/\sqrt{A_{0,i}}$. But we compute the target shape index in two different ways; in one case the shape index definition is based on the average cell area, denoted as $\tilde{p}_{0,i} = P_{0,i}/\sqrt{\langle A_i \rangle}$. In this case, $\langle A_i \rangle$ is set to 1, simplifying $\tilde{p}_{0,i}$ to $P_{0,i}$ (green data). In the other case we compute it based on the target areas of cells as in the main text, $p_{0,i} = P_{0,i}/\sqrt{A_{0,i}}$ (black data).

have an impact on the transition point, in contrast to the behavior observed when changing the width of the p_0 distribution. The transition point is illustrated by the black data in Fig. S5 and main text Fig. 3(b). In other words, due to the arguments above, both non-dimensionalizations give the same results up to an arbitrary energy constant. However, because in heterogeneous systems the individual $\sqrt{A_{0,i}}$ values can affect tensions, there is the possibility that changing the width of the area distribution could affect the rigidity transition point. As shown in Fig. S5, if one defines a dimensionless target shape index $\tilde{p}_{0,i} = P_{0,i}/\sqrt{\langle A_i \rangle}$, the rigidity transition shifts to lower values as a function of the width σ_{a_0} (green data). But, if one uses the dimensionless target shape index $p_{0,i} = P_{0,i}/\sqrt{A_{0,i}}$, as we have done throughout the manuscript, then the rigidity transition point is constant in those units (black data). This implies that the enhanced rigidity, as elucidated in Ref. [28], results from the heterogeneity in target shape indices ($p_{0,i} = P_{0,i}/\sqrt{A_{0,i}}$), rather than stemming from variations in $P_{0,i}$.

Details of tension percolation analysis

The rigidity transition in vertex models is governed by edge tensions. When the system is in the solid regime, the geometric incompatibility between the current and target cell perimeters leads to the formation of a tensional cluster that spans the entire tissue. The mechanical stability of tissue is due to the presence of this percolated

cluster. However, in the regime characterized by a large target shape factor, the tensional cluster fails to percolate, resulting in a fluid-like behavior of the tissue with a zero shear modulus. The transition point at which the tissue undergoes this rigidity change can be estimated using either tension percolation analysis or by examining the shear modulus.

To investigate tension percolation in our models, we begin by calculating the tensions, T_{ij} , on all edges ij between cells i and j

$$T_{ij} = 2K_{P,i}(P_i - P_{0,i}) + 2K_{P,j}(P_j - P_{0,j}). \quad (\text{S15})$$

Edges with tensions below a certain threshold, set here at 10^{-6} , are considered to have zero tension (varying this small threshold has no significant effect on our results). We then identify the largest connected cluster of edges that have non-zero tensions. The system is classified as rigid if the linear size of this rigid tension cluster surpasses the dimensions of our simulation box. The linear size of this cluster is determined by $\max(\max(x_v) - \min(x_v), \max(y_v) - \min(y_v))$, where v denotes a vertex within this largest rigid cluster. By adjusting the average $\langle p_0 \rangle$ and examining the percolation of edge tensions, we are able to estimate the critical point of rigidity transition, denoted as p_0^* . To validate the tension-driven rigidity mechanism in our model, we compare the critical point derived from our percolation analysis with the results from shear modulus calculations, as shown in Fig. 1b. This agreement reinforces the idea that edge tensions are pivotal in governing the rigidity transition in the model, both when learning degrees of freedom are absent and present.

The effect of the width of p_0 distribution on shear modulus G

The shear modulus G in vertex models depends not only on the average target shape factor $\langle p_{0,i} \rangle$ but also on its polydispersity. Li et al., 2019 [28], demonstrated that when tissues are minimized with respect to only physical degrees of freedom (i.e., vertex positions), the rigidity transition point increases with the standard deviation of the $\{p_{0,i}\}$ distribution. As we explore in the main text, incorporating $\{p_{0,i}\}$ as additional degrees of freedom in our energy minimization shifts the rigidity transition to lower values, regardless of the standard deviation of these degrees of freedom. Figure S6 shows how G varies with the average target shape factors, which are sampled from a normal distribution with different standard deviations σ (as specified in the legend).

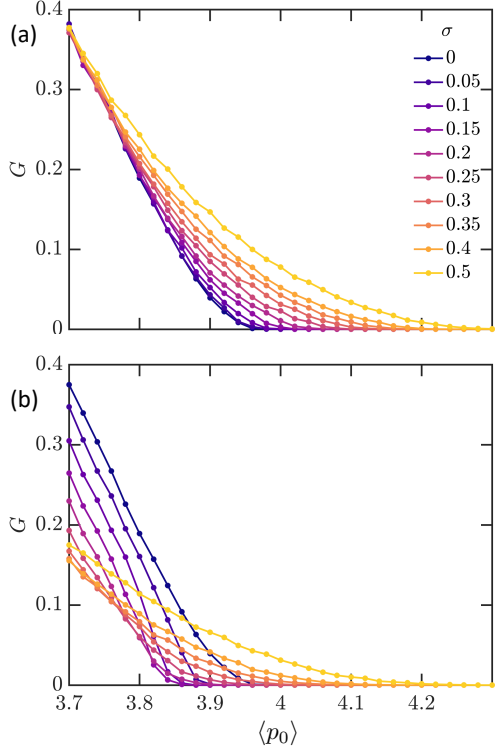


FIG. S6. The effect of standard deviation of $p_{0,i}$ distribution σ on shear modulus G . (a) Shear modulus versus the average target shape factor for various values of the standard deviation as shown in the legend. These results are for tissues that are energy-minimized with respect to only physical degrees of freedom, i.e., vertex positions. (b) Same as (a) but in presence of learning degrees of freedom $\{p_{0,i}\}$ using zero temperature swap method.

Comparing the initial and final distributions

Incorporating new degrees of freedom into our tissue models necessitates careful management of their distributions to avoid trivial or unphysical outcomes post energy minimization. For example, adding cell stiffness parameters $\{k_{p,i}\}$ as degrees of freedom without any constraints on their distribution can result in tissues unrealistically driving these parameters to negative values. To mitigate this, our minimization process includes constraints on the distribution of these new degrees of freedom. This is achieved by fixing a certain number of distribution moments, as explained in the sections above. It is important to note, though, that deviations between the initial and final distributions are inevitable following our constrained minimization approach. These deviations tend to increase with fewer constrained moments. Figure S7 compares the initially set and the resultant distributions after applying constraints on six moments, specifically $\{-3, -2, -1, 1, 2, 3\}$. To ensure that possible variations in distributions do not impact our findings, we employed a zero-temperature swap minimization method (as ex-

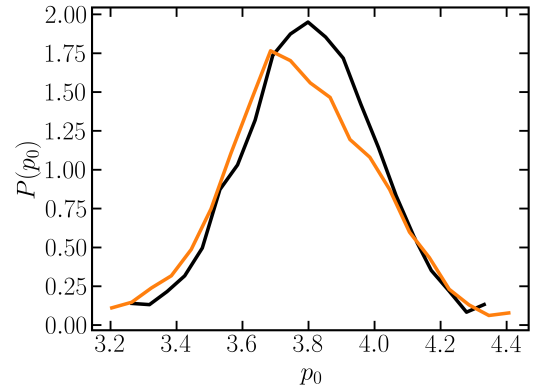


FIG. S7. Distributions of target shape factors $\{p_{0,i}\}$ before (black) and after (orange) constrained minimization with $\langle p_0 \rangle = 3.8$ and $\sigma = 0.2$. Here, we fixed 6 different moments of the distribution during our minimization.

plained in the above sections, as well). This technique precisely maintains the distribution fixed during energy minimization, relying solely on cell shuffling to achieve the lowest energy configuration.

Correlations

To decipher the observed nonmonotonic variation in the rigidity transition point relative to the standard deviation σ of the p_0 or a_0 distributions, we investigated the correlations between p_i and $p_{0,i}$, as well as between a_i and $a_{0,i}$. These correlations were analyzed both when p_0 or a_0 were and were not included as new degrees of freedom. To measure these correlations, we employed Pearson's correlation coefficient, symbolized as ρ . Pearson's correlation coefficient quantifies the relationship between two data sets and is calculated by

$$\rho(x, y) = \frac{\sum (x_i - \bar{x})(y_i - \bar{y})}{\sqrt{\sum (x_i - \bar{x})^2 \sum (y_i - \bar{y})^2}}, \quad (\text{S16})$$

where x_i and y_i represent individual data points, while \bar{x} and \bar{y} denote their respective average values. Figure S8 exhibits the correlation patterns for different σ values. Notably, for higher $\sigma \gtrsim 0.15$, a strong correlation exists between p_i and $p_{0,i}$, even without considering $p_{0,i}$ as new degrees of freedom. Consequently, introducing these new DOF has minimal impact on exploring the tissue's energy landscape. This leads to a less pronounced shift in the rigidity transition point as the permitted fluctuations in $p_{0,i}$ increase a threshold $\sigma \approx 0.15$. A similar trend is observed when target areas $a_{0,i}$ are introduced as new DOFs, while maintaining a uniform target shape factor $p_{0,i} = p_0$ (refer to Fig. S8c and d).

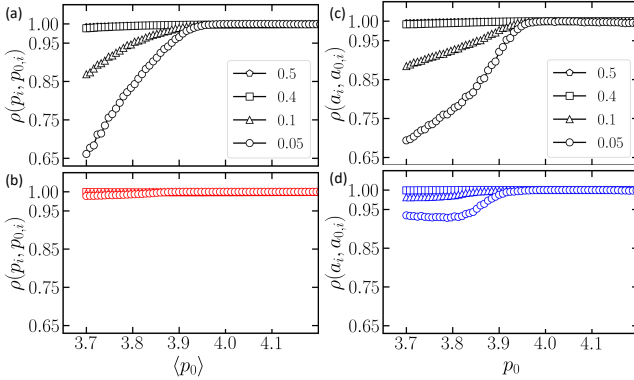


FIG. S8. The Pearson’s correlation coefficient behavior. (a) $\rho(p_i, p_{0,i})$ versus the average target shape factor for different values of the standard deviation of the p_0 distribution as shown in the legend. Here, the system’s energy is minimized only with respect to the physical degrees of freedoms, i.e., vertex positions. (b) Same as (a) but the target shape factors $p_{0,i}$ are added as new DOF in the energy minimization. (c) Showing the correlations of target areas $a_{0,i}$ and current cell areas a_i in tissues without adding target areas as DOF and at uniform target shape factors $p_{0,i} = p_0$. (d) Same as (c) but $a_{0,i}$ are added as new DOF in the minimization process.

Structural features of tissues

To decipher the difference between microstructure of tissues with and without learning degrees of freedom, we study the structural features such as the pair correlation function $g(r)$ and the hexatic order parameter. We compute $g(r)$ based on the cell centers that are calculated as center of masses of cell vertices in our vertex model. Figure S9 shows the behavior of $g(r)$ for systems with and without adding learning degrees of freedom $\{p_{0,i}\}$. In presence of $\{p_{0,i}\}$ DOF, tissues show sharper peaks in their pair correlation function depicting a more ordered structure. This effect becomes more pronounced near the transition point (Fig. S9).

To further quantify the structural differences, we study the hexatic order parameter for tissues with and without $\{p_{0,i}\}$ DOF. The local hexatic order parameter of cell k

is computed as following

$$\psi_k = \frac{1}{n_l} \sum_{\langle kl \rangle} e^{6i\theta_{kl}}, \quad (\text{S17})$$

where n_l is the number of neighbors for cell k , θ_{kl} is the angle of the vector between cells k and l with respect to the positive x -axis, and i is the imaginary number. The tissue-scale hexatic order parameter is calculated by averaging these ψ_k over all cells $\Psi = \frac{1}{N} \sum_k \psi_k$. Consistent with our $g(r)$ results, we find larger values of this hexatic order parameter when $\{p_{0,i}\}$ DOF are present in tissues, attributed to the localized regions with strong hexatic ordering. Notably, there exists a positive correlation between the local hexatic order of cell i and the quantity

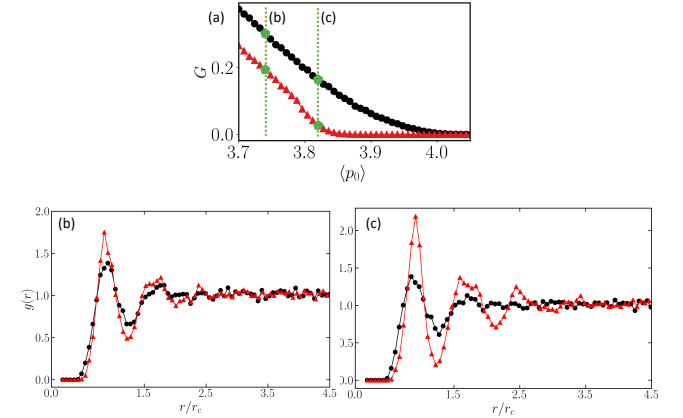


FIG. S9. Comparison of pair correlation function $g(r)$ for tissues with and without learning degrees of freedom. (a) The linear shear modulus versus the average target shape factor with a standard deviation of $\sigma = 0.15$ of $\{p_{0,i}\}$ distribution. The black (red) data points correspond to minimized-states without (with) including $\{p_{0,i}\}$ DOF. (b) $g(r)$ for the same average target shape factor $\langle p_0 \rangle$ (highlighted in the top plot of shear modulus). The dark circles (red triangles) correspond to tissues without (with) adding $\{p_{0,i}\}$ degrees of freedom. The x -axis is re-scaled with the typical half distance between cells. (c) Similar as (b) but for a higher value of $\langle p_0 \rangle$, as shown in the top plot. We used a system size of $N = 300$ cells.

$p_i - p_{0,i}$. Consequently, this large hexatic ordering actively inhibits the percolation of tensional edges, causing a downward shift in the critical threshold p_0^* (Fig. S10).

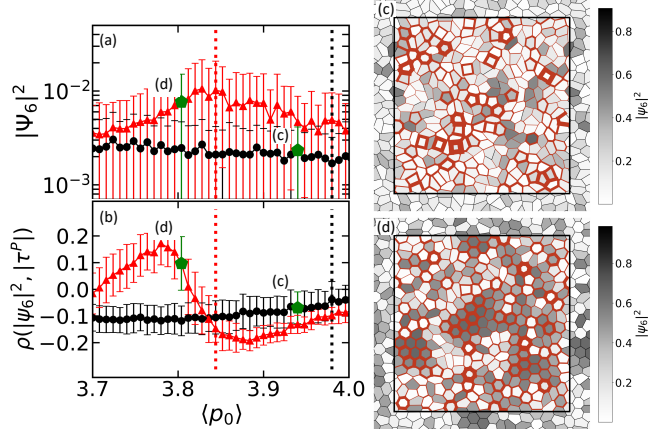


FIG. S10. Comparison of structural order with and without preferred perimeters as learning degrees of freedom. (a) Hexatic order parameter $|\Psi_6|^2$ vs. the average target shape index $\langle p_0 \rangle$. Red triangles are tissues with learning degrees of freedom and black circles are tissues with only physical degrees of freedom. (b) Pearson correlation coefficient between the local hexatic order of cells and the absolute value of the cell-scale tension ($\tau^P = p - p_0$). The vertical dashed lines indicate the rigidity transition point for each system. (c) and (d): Snapshots of tissues at average target shape indices highlighted in green in (a) and (b). Snapshot (c) showcases the structure of a tissue without learning degrees of freedom, while (d) is after learning in (p_0) . Cells are color-coded based on their local hexatic order, and edge tensions are shown in red, with thickness proportional to the tension.